Applications of Dense Media Radiative Transfer Theory for Passive Microwave Remote Sensing of Foam Covered Ocean

Jianjun Guo, Leung Tsang, *Fellow, IEEE*, William Asher, Kung-Hau Ding, and Chi-Te Chen

***Abstract*—The effect of the foam covered ocean surface on the passive microwave remote sensing measurements is studied based on the electromagnetic scattering theory. In fomulating an electromagnetic scattering model, we treat the foam as densely packed sticky air bubbles coated with thin seawater coating. The layer of foam covers the ocean surface that has air bubbles. We then use dense media radiative transfer (DMRT) theory with quasi-crystalline approximation (QCA) for densely distributed sticky moderate size particles to calculate the brightness temperatures of the foam-covered ocean surface. Results are illustrated for 19 GHz and 37 GHz and for both vertical and horizontal polarizations as a function of foam microstructure properties and foam layer thickness. Comparisons are also made with experimental measurements.**

***Index Terms*—Dense media radiative transfer, electromagnetic wave scattering, microwave emissivity.**

I. Introduction

To estimate the effect of the foam above the ocean surface on the passive microwave remote sensing measurements, various empirical microwave emissivity models were used [1]–[6]. Williams [1] measured emissivities of foam in a waveguide and found that at X-band, the emissitivity of foam depends strongly on the thickness of the foam layer. Wilheit's model [2] treats foam as having neither polarization nor viewing angle dependence. In Pandey's empirical emissivity model [3], the effect of foam was taken into account by coupling theoretical expressions of specular ocean surface emissivity with empirical expressions from ocean tower observations and from the analysis of published measurements. Smith [4] described the brightness temperature over foam-covered ocean as a function of incidence angle and frequency. He related the emissivities of foam at the three channels (vertical polarization at 19 GHz and both polarizations at 37 GHz) to one another by linear regression. Stogryn [5] used a least squares fit of a polynomial to the data of measurements and derived an expression for the foam emissivity as a function of incidence angle and frequency. All these models are empirical fitting procedures using experimental data. The empirical models do not take into account the physical microstructure properties of foam and the foam layer thickness.

It is known that foam on the ocean surface can affect the brightness temperatures measured by microwave radiometers. However, there is relatively little known definitively concerning how foam affects such fundamental parameters like the drag coefficient or the impact of foam on the retrieval of the ocean surface wind vector from satellite-mounted microwave instruments. This gap in knowledge is due in large part to the difficulty in making measurements at high wind speeds, when significant foam coverage is present. Understanding how foam increases microwave emissivity, and developing quantitative emissivity models for a foam-covered water surface, would be of great help in evaluating radiometer performance at high wind speeds.

The subject of foam dynamics has attracted attention recently. Controlled experiments are performed for foam dynamics and microwave emissivity measurements [6]. The microstructures of foam are also studied [7]. In this paper, we apply the recently developed dense media radiative transfer (DMRT) theory [8] based on sticky particle model to analyze this problem, taking into account the physical microstructure properties of foam and the foam layer thickness.

We model the foam as densely packed sticky air bubbles coated with thin seawater coating. The model of medium with densely distributed coated particles of moderate size can be used. In the past, both theoretical and experimental studies [9], [10] of the propagation and scattering of waves in dense media show that the assumption of independent scattering is not valid and the correlated scattering effects and coherent near field interaction effects must be taken into account.

The quasi-crystalline approximation (QCA) accounts for the pair distribution function of the particle positions and coherent wave interactions [11]. The Percus–Yevick equation, which compares well with the Monte Carlo simulations [12], is used to describe the pair distribution functions [11]. The scattering results of QCA also compare well with the Monte Carlo simulations of exact solutions of Maxwell's equations [10] of randomly distributed finite size spheres. Recently, we have extended the dense media theory to include cases when the particles have sticky force that make them adhere to form aggregates [8]. A key difference between sticky particle model and nonsticky particle model is the varied frequency dependence of scattering by changing the stickiness parameter τ.

We will focus on the foam impact. By using the distorted Born approximation with QCA, we calculate numerical results

Manuscript received June 8, 1999; revised November 13, 2000. This work was supported by the Office of Naval Research under Grant N00014-99-1-0190.

J. Guo, L. Tsang, and C.-T. Chen are with the Department of Electrical Engineering, University of Washington, Seattle, WA 98195-2500 USA.

W. Asher is with the Applied Physics Laboratory, University of Washington, Seattle, WA 98195 USA.

K.-H. Ding is with the Air Force Research Lab, Sensors Directorate/SNHE, Hanscom AFB, MA 01731-2909 USA.

Publisher Item Identifier S 0196-2892(01)03830-X.

of the complex effective propagation constants, scattering coefficients and phase matrix, of densely packed air bubbles coated with sea water. The brightness temperature of foam-covered ocean surface can be simulated. We describe the dynamic properties of foam in Section II. In Section III, the QCA theory for densely packed coated particles of moderate sizes is presented. For particles of moderate size, the QCA equations are formulated in terms of the T-matrix formulism and utilizing vector spherical waves as basis functions. Also, we discuss the pair distribution functions of sticky particles of multiple sizes based on the Percus–Yevick pair distribution functions. In Section IV, the DMRT theory is discussed. Derived from QCA, the DMRT theory describes the scattering, absorption and emission of a dense medium and relates the physical parameters of air bubbles coated with sea water in foam, such as the size, density and coating thickness, and layer thickness of the foam, to the brightness temperatures. The theoretical results of brightness temperatures with typical parameters of foam in passive remote sensing at 19 GHz and 37 GHz are illustrated numerically in Section V. Comparisons are also made with experimental measurements for vertical and horizontal polarizations [6].

II. Dynamic Description of Foam

In order to model the microwave radiometric properties of foam, it is critical to have an accurate model for the physical structure of the bubbles therein. Foam on a water surface is a dynamic system, and the defining physical properties such as mean bubble size and liquid water content are functions of the age of the foam. In general, the mean bubble size increases with age as bubbles coalesce and the water content decreases as water drains from the interstitial spaces [7]. In addition, the shape of the bubbles changes from nearly spherical for very young foams with relatively large liquid water content to polyhedrons for aged foams with small amounts of water in the interstitial spaces. Modeling the radiometric properties of foam is greatly simplified if it can be assumed that foam on the ocean surface is composed of nearly spherical bubbles. It is also necessary to have realistic values for the foam void fraction (i.e., the ratio of the volume of air to the total volume of the foam) and mean bubble size.

Fig. 1 is a video photograph of the bubble structure of foam on the ocean surface. The image was acquired using a partially submerged underwater CCD video camera equipped with a macro telecentric lens whose focal plane lay precisely at the front window of the camera housing. The overall thickness of the foam layer was on the order of 5 cm and it is estimated that this image was acquired in the bottom half of the foam layer. Because the foam is formed from bubbles rising to the surface from below and the lifetime of the foam layer was on the order of 4 s, this image is therefore of foam having a mean age of under 2 s. In agreement with previous data on the bubble structure of young water-based foams [7], the majority of bubbles are nearly spherical and the average thickness of the interstitial water layer between bubbles in the foam is seen to be on the order of 80 μm. Furthermore, digital image analysis of 20 similar foam images showed that the mode of the bubble size distribution is approximately 500 μm. Based on these numbers, the void fraction of the foam is on the order of 0.75 (i.e., 75% of the total volume of the foam is air). These values were used in formulating the physical model for the foam used in the electromagnetic scattering calculations.

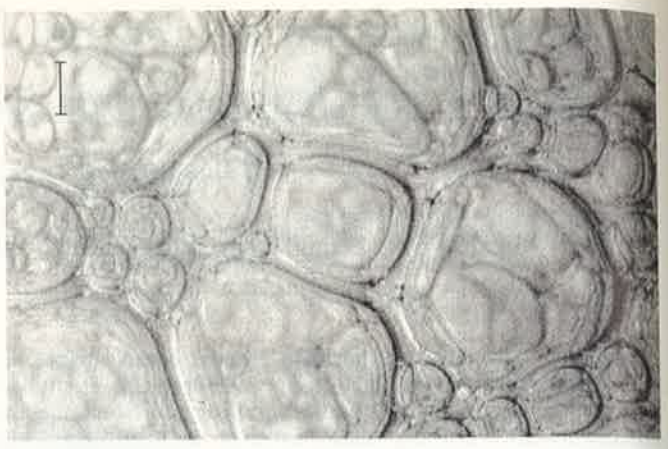

Fig. 1. Video microphotograph of bubble structure in foam on the surface of the ocean.

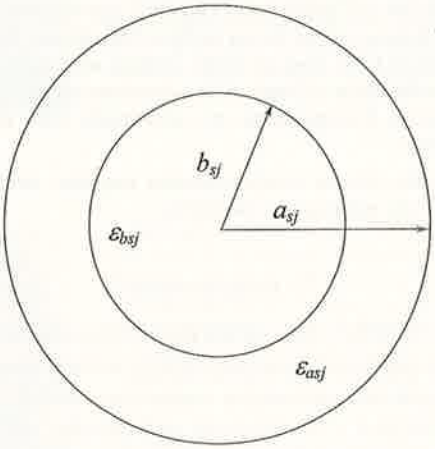

Fig. 2. Spherical dielectric coated particle. b_{sj} and a_{sj} are the inner and outer radii of spherical shells, respectively. $\varepsilon_{b_{sj}}$ and $\varepsilon_{a_{sj}}$ are permittivities of the materials in the core and within the shell, respectively.

III. Quasi-Crystalline Approximation Formulation for Media with Moderate Size Coated Particles

Consider a distribution of N coated particles centered at $\overline{r_1}, \overline{r_2}, \ldots, \overline{r_N}$ in a volume V. We assume that there are L species of coated particles in the medium. The physical and geometric structure of a spherical dielectric coated particle is shown in Fig. 2, where s_j denotes that the coated particle is of the jth species. The random distributed coated particles need not be identical in size, permittivity and the thickness of the coating. However, interpenetration of particles is not allowed. Let the incident wave impinging in the direction of $\overline{k_i}$. The Foldy-Lax multiple scattering equation can be written in matrix form as

$$\overline{w}^{(j)} = \sum_{\substack{l=1 \\ l \neq j}}^{N} \overline{\overline{\sigma}}(k\overline{r_j r_l}) \overline{\overline{T}}^{(l)} \overline{w}^{(l)} + e^{i(\overline{k_i} \cdot \overline{r_j})} \overline{a}_{\text{inc}} \tag{1}$$

where

$\overline{w}^{(j)}$ and $\overline{w}^{(l)}$ exciting field coefficients of the jth particle and the lth particle, respectively;

$\overline{\overline{T}}^{(l)}$ T-matrix of the lth particle;

$\overline{a}_{\text{inc}}$ incident field coefficient.

Equation (1) can be interpreted as the field exciting the jth particle is the sum of incident wave and the scattered wave from all other particles. The matrix $\overline{\overline{\sigma}}(k\overline{r_j r_l})$ is the matrix that describes the vector translation formula transforming spherical waves centered at $\overline{r_l}$ to spherical waves centered at $\overline{r_j}$. By taking the conditional average by holding position $\overline{r_j}$ fixed, we have

$$\begin{aligned}\overline{w}(\overline{r_j}) =& E_j\left(\overline{w}^{(j)}\right)\\ =& \sum_{\substack{l=1\\ l\neq j}}^{N}\int d\overline{r_l}\,\overline{\overline{\sigma}}(k\overline{r_j r_l})p(\overline{r_l}|\overline{r_j})\overline{\overline{T}}^{(l)}E_{lj}\left(\overline{w}^{(l)}\right)\\ &+ e^{i(\overline{k_{id}}\cdot\overline{r_j})}\overline{a}_{\text{inc}}\end{aligned} \tag{2}$$

where

E_j conditional average given the position and state of the jth particle;

$p(\overline{r_l}|\overline{r_j})$ conditional probability of finding the lth particle at $\overline{r_l}$ given the jth particle at $\overline{r_j}$;

E_{lj} conditional average given the properties and positions of particles l and j.

Based on the QCA

$$E_{lj}\left(\overline{w}^{(l)}\right) \simeq E_l\left(\overline{w}^{(l)}\right) \equiv \overline{w}(\overline{r_l}) \tag{3}$$

we can obtain the averaged exciting field as follows:

$$\begin{aligned}\overline{w}^{(s_j)}(\overline{r_j}) =& \sum_{s_l=1}^{L} n_{s_l}\int_{V_{lj}} d\overline{r_l}\,g_{s_l s_j}(\overline{r_l}-\overline{r_j})\overline{\overline{\sigma}}(k\overline{r_j r_l})\overline{\overline{T}}^{(l)}\\ &\times \overline{w}^{(s_l)}(\overline{r_l}) + e^{i(\overline{k_{id}}\cdot\overline{r_j})}\overline{a}_{\text{inc}}\end{aligned} \tag{4}$$

where

n_{s_l} number of particles per unit volume of the L species;

$\overline{w}^{(s_j)}(\overline{r_j})$ conditional average of the exciting field of particles at $\overline{r_j}$ of species s_j;

$\overline{\overline{T}}^{(l)}$ matrix representation of the T matrix of species s_l;

$g_{s_l s_j}(\overline{r_l}-\overline{r_j})$ cross pair distribution function of two species s_l and s_j;

$\overline{a}_{\text{inc}}$ column matrix representing the coefficient of the incident wave when expanded into spherical waves.

The integral equation in (4) can be solved by using vector spherical wave expansions. They lead into two sets of equations, the Lorentz–Lorenz law and the Ewald–Oseen extinction theorem [13].

The conditional averaged exciting field coefficients obey the following homogeneous system of equations (Lorentz–Lorenz law). Let $\overline{w}^{(s_j)}(\overline{r_j})$ be expanded into vector spherical waves with $Y_\nu^{(s_j)(M)}$ and $Y_\nu^{(s_j)(N)}$ as coefficients where $\nu = 1,2,\ldots,(M)$ and (N) represents the $\overline{M}$ and $\overline{N}$ vector spherical waves, respectively

$$\begin{aligned}Y_\nu^{(s_j)(M)} =& -2\pi\sum_{s_l=1}^{L} n_{s_l}\sum_{n,p}(2n+1)S_p(k,K|R_{s_j s_l})\\ &\times\left\{a(1,n|-1,\nu|p)\,A(n,\nu,p)\,T_n^{(s_l)(M)}Y_n^{(s_l)(M)}\right.\\ &+ a(1,n|-1,\nu|p,p-1)\,B(n,\nu,p)\\ &\left.\times\, T_n^{(s_l)(N)}Y_n^{(s_l)(N)}\right\}\end{aligned} \tag{5}$$

$$\begin{aligned}Y_\nu^{(s_j)(N)} =& -2\pi\sum_{s_l=1}^{L} n_{s_l}\sum_{n,p}(2n+1)S_p(k,K|R_{s_j s_l})\\ &\times\left\{a(1,n|-1,\nu|p,p-1)\,B(n,\nu,p)\right.\\ &\times T_n^{(s_l)(M)}Y_n^{(s_l)(M)} + a(1,n|-1,\nu|p)\\ &\left.\times\, A(n,\nu,p)\,T_n^{(s_l)(N)}Y_n^{(s_l)(N)}\right\}.\end{aligned} \tag{6}$$

In (5) and (6)

$$\begin{aligned}S_p(k,K|R_{s_j s_l}) =& -\frac{R_{s_j s_l}^2}{K^2-k^2}\left[kh_p'(kR_{s_j s_l})j_p(KR_{s_j s_l})\right.\\ &\left.- Kh_p(kR_{s_j s_l})\,j_p'(kR_{s_j s_l})\right]\\ &+\int_{R_{s_j s_l}}^{\infty} drr^2\left[g_{s_j s_l}(r)-1\right]\\ &\times h_p(kr)\,j_p(Kr)\end{aligned} \tag{7}$$

where $A(n,\nu,p)$ and $B(n,\nu,p)$ are coefficients defined in [11, p. 496], $a(1,n|-1,\nu|p)$ and $a(1,n|-1,\nu|p,p-1)$ are terms of Wigner $3j$ symbols defined in [11, pp. 449–450]; $K = K'+iK''$ is the effective propagation constant; j_p and j_p' are spherical Bessel function and its derivative; h_p and h_p' are spherical Hankel function and its derivative. The scattering coefficients $T_n^{(M)}$ and $T_n^{(N)}$, for coated spheres of lth species with outer radius a_{s_l}, inner radius b_{s_l}, core wavenumber k_{b_l} and shell wavenumber k_{a_l}, are those of Mie scattering T-matrix coefficients expressed by [14] in (8) and (9), shown at the bottom of the page,

$$T_n^{(s_l)(M)} = -\frac{[\rho_{s_l}j_n(\rho_{s_l})]'[j_n(\varsigma_{s_l})+B_n^{s_l}y_n(\varsigma_{s_l})] - \{[\varsigma_{s_l}j_n(\varsigma_{s_l})]'+B_n^{s_l}[\varsigma_{s_l}y_n(\varsigma_{s_l})]'\}j_n(\rho_{s_l})}{[\rho_{s_l}h_n(\rho_{s_l})]'[j_n(\varsigma_{s_l})+B_n^{s_l}y_n(\varsigma_{s_l})] - \{[\varsigma_{s_l}j_n(\varsigma_{s_l})]'+B_n^{s_l}[\varsigma_{s_l}y_n(\varsigma_{s_l})]'\}h_n(\rho_{s_l})} \tag{8}$$

$$T_n^{(s_l)(N)} = -\frac{[\rho_{s_l}j_n(\rho_{s_l})]'\varsigma_{s_l}^2[j_n(\varsigma_{s_l})+A_n^{s_l}y_n(\varsigma_{s_l})] - \{[\varsigma_{sl}j_n(\varsigma_{s_l})]'+A_n^{s_l}[\varsigma_{sl}y_n(\varsigma_{s_l})]'\}\rho_{s_l}^2 j_n(\rho_{s_l})}{[\rho_{s_l}h_n(\rho_{s_l})]'\varsigma_{s_l}^2[j_n(\varsigma_{s_l})+A_n^{s_l}y_n(\varsigma_{s_l})] - \{[\varsigma_{sl}j_n(\varsigma_{s_l})]'+A_n^{s_l}[\varsigma_{sl}y_n(\varsigma_{s_l})]'\}\rho_{s_l}^2 h_n(\rho_{s_l})} \tag{9}$$

where

$$B_n^{s_l} = -\frac{[\xi_{s_l} j_n(\xi_{s_l})]' j_n(\eta_{s_l}) - [\eta_{s_l} j_n(\eta_{s_l})]' j_n(\xi_{s_l})}{[\xi_{s_l} y_n(\xi_{s_l})]' j_n(\eta_{s_l}) - [\eta_{s_l} j_n(\eta_{s_l})]' y_n(\xi_{s_l})} \tag{10}$$

$$A_n^{s_l} = -\frac{[\xi_{s_l} j_n(\xi_{s_l})]' \eta_{s_l}^2 j_n(\eta_{s_l}) - [\eta_{s_l} j_n(\eta_{s_l})]' \xi_{s_l}^2 j_n(\xi_{s_l})}{[\xi_{s_l} y_n(\xi_{s_l})]' \eta_{s_l}^2 j_n(\eta_{s_l}) - [\eta_{s_l} j_n(\eta_{s_l})]' \xi_{s_l}^2 y_n(\xi_{s_l})} \tag{11}$$

and $y_n(\cdot)$ is the spherical Neumann function. The symbols ρ_{s_l}, ξ_{s_l}, ς_{s_l}, and η_{s_l} are defined as $\rho_{s_l} = ka_{s_l}$, $\xi_{s_l} = k_{a_l} b_{s_l}$, $\varsigma_{s_l} = k_{a_l} a_{s_l}$, and $\eta_{s_l} = k_{b_l} b_{s_l}$, respectively.

The ratios of exciting field coefficients $Y_\nu^{(s_j)(M)}$ and $Y_\nu^{(s_j)(N)}$ are determined by setting the determinant of (5) and (6) equal to zero. The determinant equation gives the solution for the effective propagation constant K. They can be solved numerically by using Muller's method to search the root K. Therefore, the value of $Y_\nu^{(s_j)(M)}$ and $Y_\nu^{(s_j)(N)}$ can be determined within a single constant. The effective propagation constant K is complex, $K = K' + iK''$, and the extinction rate is $\kappa_e = 2K''$. In principle, both K' and K'' can be computed by the Lorentz–Lorenz law. However, since $K' \gg K''$, K'' calculated in this manner may not have the desired accuracy. Also, the imaginary part K'' is affected by the sticky particle pair distribution functions that have sharp peaks that may be difficult to evaluate numerically. To ensure energy conservation, we proceed as follows. We use the real part K' as calculated from (5) and (6) of Lorentz–Lorenz law. We also use the relative values of $Y_\nu^{(s_j)}$'s as determined by (5) and (6). For the single constant, it is determined by Ewald–Oseen extinction theorem. The generalized Ewald–Oseen extinction theorem is obtained by balancing the incident wave term and the term of the same phase dependence that is a result of the integral in (4). We then use the coherent exciting field to calculate the absorption coefficient. The distorted Born approximation is applied to calculate the phase matrix elements and the scattering coefficient. The phase matrix is the bistatic cross section per unit volume. In passive remote sensing, we further integrate over the azimuthal angle ϕ

$$p_{\alpha\beta}(\theta, \theta') = \int_0^{2\pi} d\phi P_{\alpha\beta}(\theta, \phi; \theta', \phi' = 0) \tag{12}$$

where $\alpha, \beta = v, h$, and $P_{\alpha\beta}$ is given by [8, eqs. (37)–(40)]. Then, the extinction coefficient is calculated by the addition of absorption and scattering coefficients.

By employing the coherent exciting field on a particle $\overline{w}^{(s_j)}(\overline{r_j})$ as solved by QCA, we can obtain the reflection coefficient which is given in [8] as

$$\begin{aligned} R = \sum_{s_j=1}^{L} \frac{2\pi n_{s_j} i}{k k_{iz} (K_z + k_{iz})} \sum_n (-1)^n \frac{(2n+1)}{n(n+1)} \\ \times \left\{ T_n^{(s_j)(M)} Y_n^{(s_j)(M)(V)} \frac{P_n^1(\cos(\theta_i + \theta_t))}{\sin(\theta_i + \theta_t)} \right. \\ + T_n^{(s_j)(N)} Y_n^{(s_j)(N)(V)} \left[n(n+1) P_n(\cos(\theta_i + \theta_t)) \right. \\ \left. \left. + \cot(\theta_i + \theta_t) P_n^1(\cos(\theta_i + \theta_t)) \right] \right\} \end{aligned} \tag{13}$$

where

P_n^1 associated Legendre polynomial of nth order and degree 1;

P_n Legendre polynomial;

θ_i and θ_t incident and transmitted angles, respectively.

And then we can get the absorption coefficient as follows:

$$\begin{aligned} \kappa_a = \frac{2\pi}{k^2 |1 - R|^2} \sum_{s_j=1}^{L} n_{s_j} \sum_n (2n+1) \left[\left| Y_n^{(s_j)(M)(V)} \right|^2 \right. \\ \times \left(-\operatorname{Re} T_n^{(s_j)(M)} - \left| T_n^{(s_j)(M)} \right|^2 \right) + \left| Y_n^{(s_j)(N)(V)} \right|^2 \\ \left. \times \left(-\operatorname{Re} T_n^{(s_j)(N)} - \left| T_n^{(s_j)(N)} \right|^2 \right) \right]. \end{aligned} \tag{14}$$

The scattering coefficient can be calculated by the following

$$\begin{aligned} \kappa_s &= \int_0^{\pi} d\theta \sin\theta \left(p_{\mathrm{vv}}(\theta, \theta') + p_{\mathrm{hv}}(\theta, \theta') \right) \\ &= \int_0^{\pi} d\theta \sin\theta \left(p_{\mathrm{vh}}(\theta, \theta') + p_{\mathrm{hh}}(\theta, \theta') \right). \end{aligned} \tag{15}$$

The extinction coefficient is $\kappa_e = \kappa_s + \kappa_a$ and the Albedo is $\widetilde{\omega} = \kappa_s / \kappa_e$. The effective propagation constant K is $K' + i\kappa_e/2$.

Physically, the air bubbles in the foam layer adhere to each other, which is shown in Fig. 1. To simulate the foam's effect, we use the sticky particle model in which the particles are allowed to adhere together to form clusters to better represent the physical property of the foam. The sticky particle has a stickiness parameter τ. The smaller the τ is, the more sticky the particles are. The Percus–Yevick approximation of the pair distribution function $g(r)$ for the sticky spherical particles can be solved analytically using the factorization method of Baxter [15]. The calculations of $g(r)$ are given by equations in [16]. In the following sections, we use particles of identical size but with different thicknesses of coating.

IV. Dense Media Radiative Transfer Theory

Consider thermal emission from a layered medium with coated dielectric particles embedded in a background medium, as indicated in Fig. 3. The layer consisting of coated particles (in region 1) covers a half space of ocean (region 2) embedded with air bubbles. The radiative transfer (RT) equations for passive remote sensing in region 1 are in the following form:

$$\begin{aligned} \cos\theta \frac{dI_v}{dz}(\theta, z) = &-\kappa_e I_v(\theta, z) + \kappa_a CT \\ &+ \int_0^{\pi} d\theta' \sin\theta' (p_{\mathrm{vv}}(\theta, \theta') I_v(\theta', z) \\ &+ p_{\mathrm{vh}}(\theta, \theta') I_h(\theta', z)) \end{aligned} \tag{16}$$

$$\begin{aligned} \cos\theta \frac{dI_h}{dz}(\theta, z) = &-\kappa_e I_h(\theta, z) + \kappa_a CT \\ &+ \int_0^{\pi} d\theta' \sin\theta' (p_{\mathrm{hv}}(\theta, \theta') I_v(\theta', z) \\ &+ p_{\mathrm{hh}}(\theta, \theta') I_h(\theta', z)) \end{aligned} \tag{17}$$

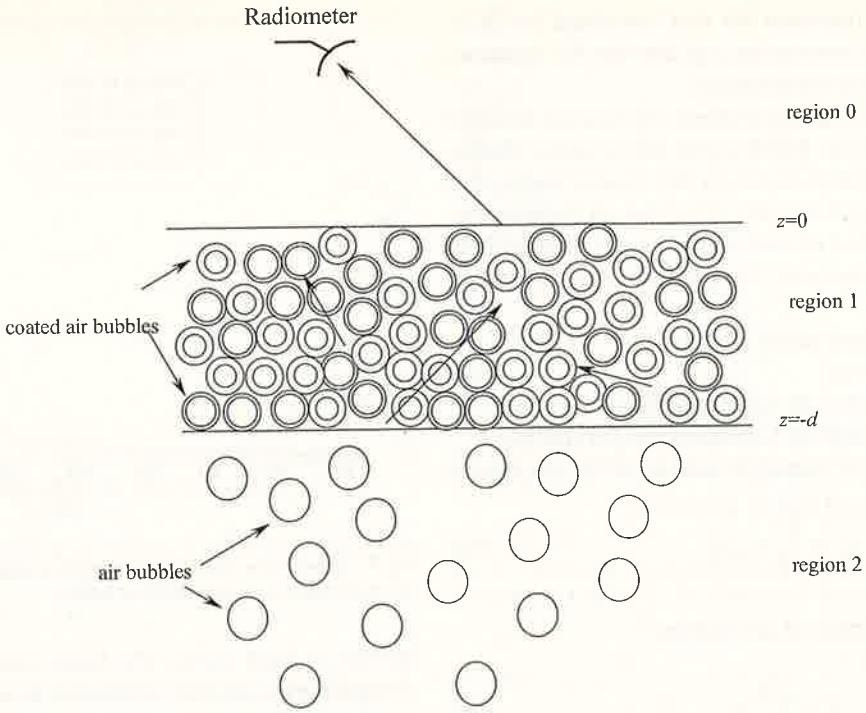

Fig. 3. Geometrical configuration for thermal emission from foam covered ocean. The foam layer is region 1 and is absoptive and scattering. Region 2 is air bubbles embedded in sea water and is absorptive.

where

C equal to $K_b K'^2/(\lambda^2 k^2)$,;
K_b Boltzman's constant;
I_v, I_h vertical and horizontal specific intensities, respectively.

The boundary conditions are the Fresnel type using the effective propagation constant for the dense medium. For the upper boundary, the air/region 1 interface at $z = 0$

$$R_v(\theta) = r_v(\theta) \tag{18}$$
$$R_h(\theta) = r_h(\theta) \tag{19}$$

where r_v and r_h are the Fresnel reflectivities with effective propagation constant K

$$r_v(\theta) = \left| \frac{k^2 \cos\theta - K' \left(k^2 - K'^2 \sin^2\theta\right)^{1/2}}{k^2 \cos\theta + K' \left(k^2 - K'^2 \sin^2\theta\right)^{1/2}} \right|^2 \tag{20}$$

$$r_h(\theta) = \left| \frac{K' \cos\theta - \left(k^2 - K'^2 \sin^2\theta\right)^{1/2}}{K' \cos\theta + \left(k^2 - K'^2 \sin^2\theta\right)^{1/2}} \right|^2. \tag{21}$$

In the lower boundary, the region 1 and region 2 interface, $z = -d$

$$R_{\rm vg}(\theta) = r_{\rm vg}(\theta) \tag{22}$$
$$R_{\rm hg}(\theta) = r_{\rm vg}(\theta) \tag{23}$$

with (24) and (25), shown at the bottom of the page, where ε_2 is the permittivity of the media in region 2. For the case of foam covered ocean, region 2 consists of air bubbles embedded in the ocean background so that we will use the effective permittivity $\varepsilon_{\rm eff2}$ of medium 2 in this set of equations, instead of ε_2. Region 2 is assumed to be absorptive. To calculate $\varepsilon_{\rm eff2}$, a simple physical model based on induced dipoles is used [13]. Let ε_w denote the permittivity of the seawater, f_a the fractional volume occupied by the air bubbles. Then the effective permittivity $\varepsilon_{\rm eff2}$, is given by the Maxwell-Garnett mixing formula

$$\varepsilon_{\rm eff2} = \varepsilon_w \frac{1 + 2 f_a y}{1 - f_a y} \tag{26}$$

where

$$y = \frac{\varepsilon_0 - \varepsilon_w}{\varepsilon_0 + 2\varepsilon_w}. \tag{27}$$

Note that the effective permittivity $\varepsilon_{\rm eff2}$ here does not include scattering attenuation which is small due to the fact that the seawater is heavily absorptive.

After solving the eigenvalue problem and imposing on the boundary conditions, the brightness temperatures in the direction θ_0, where $\theta_0 = \sin^{-1}(K' \sin\theta/k)$ is related to θ by Snells' law, are given by

$$T_{B_v}(\theta_0) = \frac{1}{C}(1 - R_v(\theta)) I_v(z = 0, \theta) \tag{28}$$
$$T_{B_h}(\theta_0) = \frac{1}{C}(1 - R_h(\theta)) I_h(z = 0, \theta). \tag{29}$$

V. Numerical Simulations of Brightness Temperature and Comparison with Experimental Measurements

In the following, we illustrate the numerical results of the brightness temperatures based on the sticky particle model. The effective propagation constant, scattering rate, extinction rate,

albedo, and the phase functions are first calculated by QCA. Consequently, these parameters are put into the RT equations to compute the brightness temperatures.

As described in the foregoing sections, the foam is modeled as densely packed sticky air bubbles with thin seawater coating and the background medium is air. In this model, region 0 is air, region 1 is foam layer consists of coated air bubbles embedded in a background of air, and region 2 consists of air bubbles and ocean as its background. The geometrical configuration is shown in Fig. 3.

We define the foam parameters as follows:

d foam layer thickness;

a_j outer radius of coated air bubbles of the jth species;

b_j inner radius of coated air bubbles of the jth species;

f_j fractional volume of coated air bubbles of the jth species

$$f_j = \frac{4\pi}{3} n_{sj} a_j^3 \tag{30}$$

f total fractional volume of air bubbles

$$f = \sum_{j=1}^{N_s} f_j \tag{31}$$

N_s number of species, we choose two in the numerical simulations;

f_w fractional volume of sea water in foam

$$f_w = \sum_{j=1}^{N_s} f_j \left[1 - \left(\frac{b_j}{a_j}\right)^3\right] \tag{32}$$

τ stickiness parameter for the sticky model;

ε_w permittivity of seawater;

T the temperature of the foam;

θ observation angle;

f_a fractional volume of air bubble in medium 2 (used in (26) to calculate $\varepsilon_{\text{eff2}}$).

Note that $a_j - b_j$ is the thickness of coating of the jth species. And we assume that the permittivity of the sea water in this layer is the same as that in foam, also they have the same temperature.

According to the microstructure of foam, f_w is about 4%. The diameter of coated air bubbles $2a_j$ ranges from 200 μm to several millimeters. The thickness of the coating of the air bubbles in foam varies. The foam extends to a layer thickness d ranging from several millimeters to several centimeters. Note that the permittivity of seawater ε_w is a function of the frequency and other physical parameters such as the temperature T and salinity. To calculate the permittivity of seawater at microwave remote sensing frequencies, we set the temperature of 284 K and salinity of 20 per thousand, and the model of Klein and Swift [17] is applied. Based on this model, the permittivity of the sea water at 19 GHz and 37 GHz are $28.9541 + i36.8340$ and $13.2444 + i24.5221$, respectively.

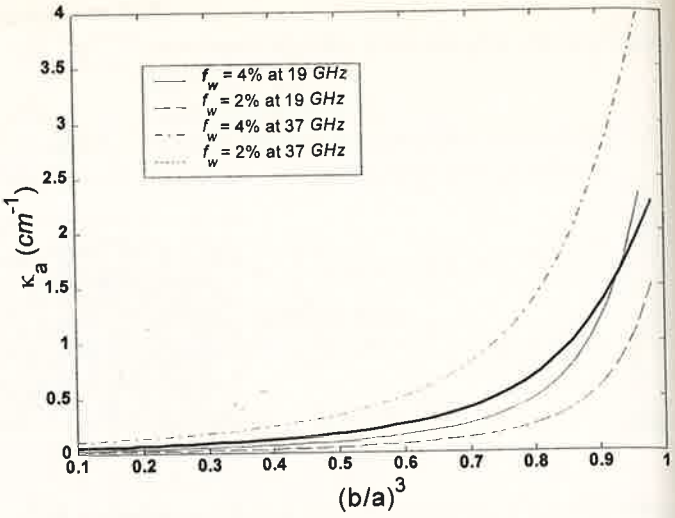

Fig. 4. Absorption coefficient as a function of the ratio of the inner radius b to the outer radius a of the coated air bubble.

First, we present the absorption coefficient dependence on the coating thickness for several f_w in Fig. 4. It is clear that, with the same water fractional volume f_w, the absorption coefficient κ_a for air bubbles with thinner coating is much larger than that of bubbles with thicker coating. Also, while keeping the coating thickness fixed, the absorption coefficient will increase with the increase of water fractional volume. On the other hand, we can see that the coated air bubble is more absorptive at 37 GHz than that at 19 GHz.

The following results show the brightness temperatures as a function of the observation angle, the thickness of the foam layer, and the size of the coated air bubbles in the foam layer. All the parameters for the simulation results shown in Figs. 5–8 are listed in Table I. For simplicity, we have used two species of coated air bubbles having identical size but with different

$$r_{\text{vg}}(\theta) = \left| \frac{(\varepsilon_2/\varepsilon_0)k^2 \cos\theta - K'\left((\varepsilon_2/\varepsilon_0)k^2 - K'^2 \sin^2\theta\right)^{1/2}}{(\varepsilon_2/\varepsilon_0)k^2 \cos\theta + K'\left((\varepsilon_2/\varepsilon_0)k^2 - K'^2 \sin^2\theta\right)^{1/2}} \right|^2 \tag{24}$$

$$r_{\text{hg}}(\theta) = \left| \frac{K' \cos\theta - \left(\varepsilon_2/\varepsilon_0 k^2 - K'^2 \sin^2\theta\right)^{1/2}}{K' \cos\theta + \left((\varepsilon_2/\varepsilon_0)k^2 - K'^2 \sin^2\theta\right)^{1/2}} \right|^2 \tag{25}$$

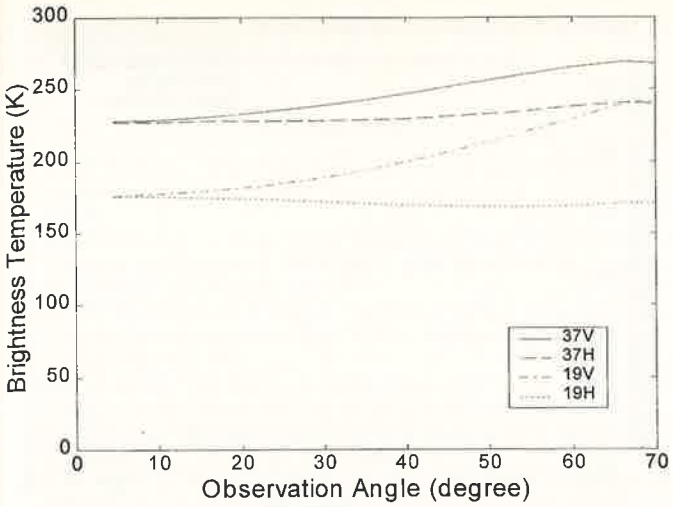

Fig. 5. Brightness temperature as a function of observation angle. The diameter of the coated air bubble is 500 μm.

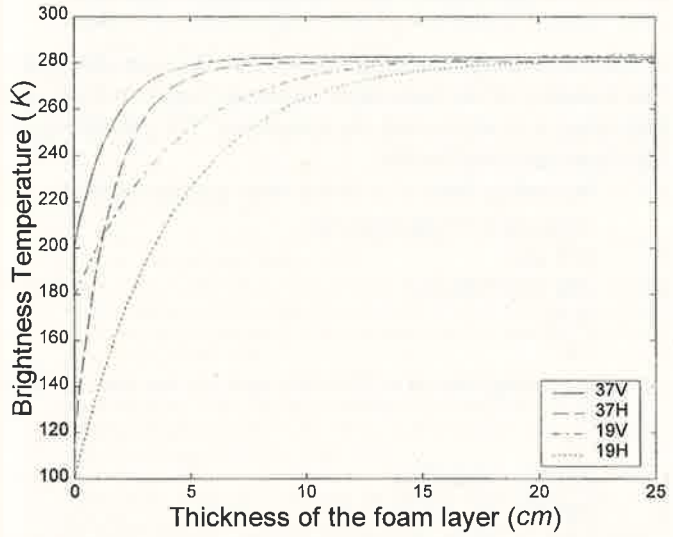

Fig. 6. Brightness temperature as a function of the thickness of the foam layer at observation angle 53°. The diameter of the coated air bubble is 500 μm.

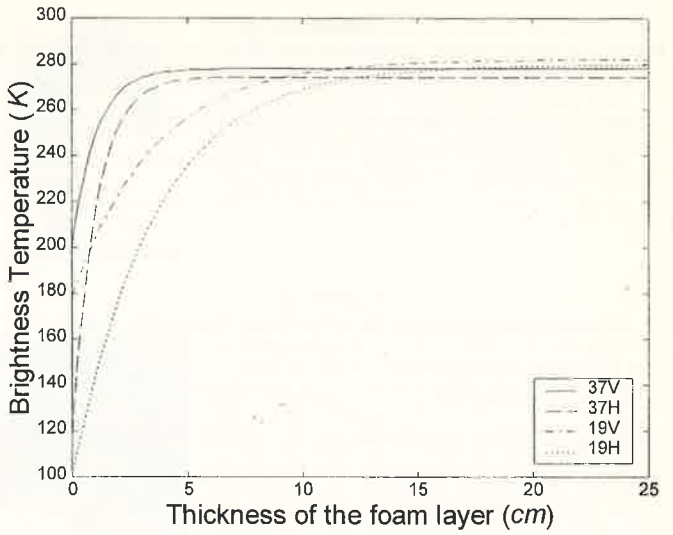

Fig. 7. Brightness temperature as a function of the thickness of the foam layer at observation angle 53°. The diameter of the coated air bubble is 1000 μm.

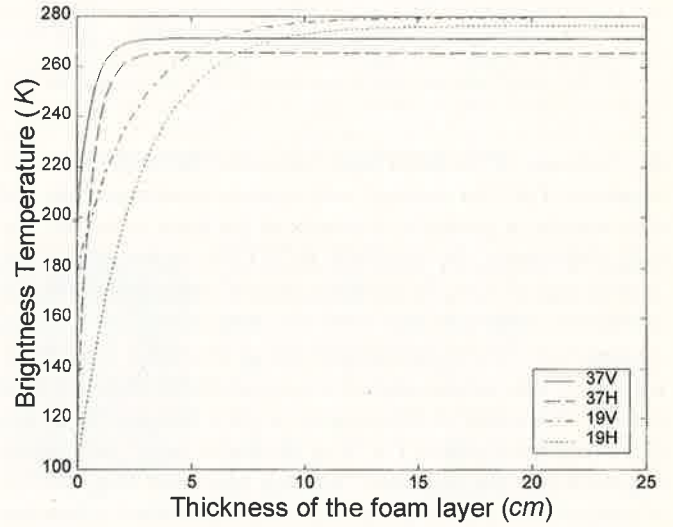

Fig. 8. Brightness temperature as a function of the thickness of the foam layer at observation angle 53°. The diameter of the coated air bubble is 1500 μm.

coating thickness and fractional volume, namely thicker coated one with small fractional volume and thinner coated one with larger fractional volume, in the foam description.

Fig. 5 shows the calculated brightness temperatures as a function of observation angle at 19 GHz and 37 GHz, for both horizontal polarization and vertical polarization, respectively. In Figs. 6–8, we plot the brightness temperatures of horizontal polarization and vertical polarization, at 19 GHz and 37 GHz also, as a function of thickness of the foam layer with different size of the coated air bubbles. The diameters of air bubbles are 500 μm, 500 μm, 1000 μm, and 1500 μm in Figs. 4–7, respectively. As the size of bubbles increases the scattering effects increases and the albedo also increases, which is reflected by the decrease of the corresponding saturated brightness temperatures. The observation angle is 53° for Figs. 5–7. Fig. 5 shows the polarization dependence as a function of viewing angles. We note that 19 GHz has a stronger polarization dependence than 37 GHz. The polarization difference are respectively 43 K and 32 K at 53° observation angle. Fig. 6 indicates that, once the brightness temperatures at 19 GHz increase to the values of that at 37 GHz, then saturations for 19 GHz take place. The frequency dependence is weak after saturation. The polarization dependence is also weak for a large thickness of foam layer of small coated air bubbles. From these three figures, we can conclude that as

TABLE I
PARAMETERS FOR THE SIMULATED RESULTS SHOWN IN FIGS. 5–8

	d	$2a$	$2b_1$	$2b_2$	f	f_w	f_a	f_1	f_2	θ
Figure 5	$2cm$	$500\mu m$	$248\mu m$	$498\mu m$	50%	4%	20%	4.5%	45.5%	0° to 90°
Figure 6	$0-25cm$	$500\mu m$	$248\mu m$	$498\mu m$	50%	4%	20%	4.5%	45.5%	53°
Figure 7	$0-25cm$	$1000\mu m$	$496\mu m$	$999\mu m$	50%	4%	20%	4.5%	45.5%	53°
Figure 8	$0-25cm$	$1500\mu m$	$744\mu m$	$1498\mu m$	50%	4%	20%	4.5%	45.5%	53°

TABLE II
NUMERICAL RESULTS FROM THE QCA-STICKY SIMULATION FOR FIGS. 5 AND 6

Parameter	Albedo	Extinction Rate κ_e/k	Effective Permittivity ε_{eff}	ka
$19GHz$	0.0080	0.0165	$1.1365 + i0.0176$	0.0995
$37GHz$	0.0377	0.0151	$1.1306 + i0.01604$	0.1937

TABLE III
NUMERICAL RESULTS FROM THE QCA-STICKY SIMULATION FOR FIG. 7

Parameter	Albedo	Extinction Rate κ_e/k	Effective Permittivity ε_{eff}	ka
$19GHz$	0.0497	0.0098	$1.1395 + i0.0105$	0.1990
$37GHz$	0.1642	0.0149	$1.1394 + i0.0159$	0.3875

TABLE IV
NUMERICAL RESULTS FROM THE QCA-STICKY SIMULATION FOR FIG. 8

Parameter	Albedo	Extinction Rate κ_e/k	Effective Permittivity ε_{eff}	ka
$19GHz$	0.1147	0.0099	$1.1481 + i0.0107$	0.2985
$37GHz$	0.3166	0.0200	$1.1579 + i0.0215$	0.5812

the thickness of the foam layer increases, the brightness temperatures of all four channels will increase correspondingly and then saturate at particular thickness of the foam layer. For vertical polarization, the saturation at 19 GHz occurs at 21.9 cm, 16.4 cm and 15.9 cm, for the three cases of coated air bubble size of 500 μm, 1000 μm, and 1500 μm, respectively. At 37 GHz, saturation of vertical polarization occurs at smaller layer thickness of 8.3 cm, 4.5 cm, and 4.0 cm, respectively. The saturation point of horizontal polarization is slightly different from that of vertical polarization. For layer thickness larger than saturation thickness, the difference between brightness temperatures of vertical polarization and horizontal polarization is a function of the size of coated air bubbles. The extinction rates, effective wavenumbers and albedo calculated from QCA for these cases are shown in Tables II–IV, respectively. It can be seen that the seawater is absorptive and absorption dominates over the extinction rates for small particle sizes. However, as the particle size increases, the albedo increases with the size of coated air bubbles. In these tables, the effective permittivity ε_{eff} of region 1 is defined as $\varepsilon_{\text{eff}} = (K/k)^2$, where K is the effective propagation constant and k is the wave number in free space.

Next, in Fig. 9 we compare the simulation results with the experimental measurements in [6]. In the experiment, brightness temperatures of vertical polarization and horizontal polarization were measured at 19 GHz. The incidence angle was set at 53°.. To reduce noise, Asher *et al.* [6] averaged the time series of brightness temperature for successive bubble plumes by using the tipping bucket to generate reproducible bubble plumes. Following the computational procedure described in the foregoing sections, we simulated the corresponding time series of brightness temperature. The experimental observation indicates that the brightness temperatures increases rapidly with a time interval of 1 s and then gradually decreases to the ocean values

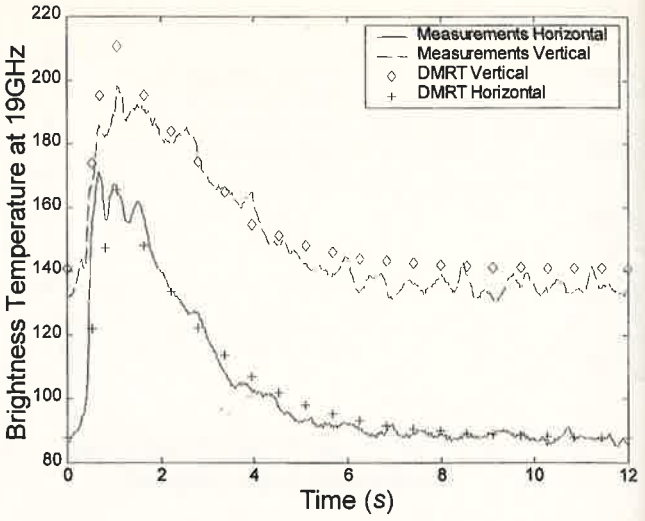

Fig. 9. Comparison between the simulation results and the measurements for the time series of the ocean surface microwave brightness temperature at 19 GHz for horizontal polarization and vertical polarization, respectively.

of brightness temperatures in about 8 s as the foam dissipates. The thickness of the foam layer increases from 0 to 2 cm, and then down to 0 which ends the simulation. The parameters for this figure are listed below.

d increasing from 0 to 2 cm very quickly and then decreasing to 0 exponentially;
$2a$ 400 μm;
$2b$ 200 μm–395 μm;
f 50%;
f_w 4%;
f_a increasing from 0 to 50% very quickly and then down to 0;
τ 0.1;
ε_w 28.9541+i36.8340;
T 284 K.

From Fig. 9, we see that the simulation results compare well with the experimental measurements. At a single time instant, the simulated brightness temperatures of vertical polarization and horizontal polarization agree well with the experimental measurements. Moreover, from the point of view of time series, the simulated brightness temperatures agree well with those of measurements. Also, the polarization dependence for the time series (corresponding to different thickness of foam layer) is well predicted by the sticky particle model.

VI. CONCLUSIONS

By formulating an electromagnetic scattering model of foam, we apply electromagnetic scattering theory and dense media radiative transfer theory to analyze the effects of foam on the passive microwave remote sensing measurements rigorously. We model the foam as densely packed sticky air bubbles coated with thin seawater coating. The DMRT for moderate size sticky particles based on QCA is applied to calculate the brightness temperatures of the foam-covered ocean surface. Numerical simulations show that the polarization and frequency dependences of brightness temperatures on microstructure properties such as foam layer thickness, foam air bubble size, coating thickness

and coated bubbles fractional volume. Simulation results are in good agreement with experimental measurements.

REFERENCES

[1] G. F. Williams, "Microwave Emissivity Measurements of Bubbles and Foam," *IEEE Trans. Geosci. Electron.*, vol. GE-9, pp. 221–224, July 1971.

[2] T. T. Wilheit Jr, "A Model for the Microwave Emissivity of the Ocean's Surface as a Function of Wind speed," *IEEE Trans. Geosci. Electron.*, vol. GE-17, pp. 244–249, Apr. 1979.

[3] P. C. Pandey and R. K. Kakar, "An Empirical Microwave emissivity Model for a Foam-Covered Sea," *IEEE J. Oceanic Eng.*, vol. OE-7, no. 3, pp. 135–140, 1982.

[4] P. M. Smith, "The Emissivity of Sea Foam at 19 and 37 GHz," *IEEE Trans. Geosci. Remote Sensing*, vol. 26, pp. 541–547, Sept. 1988.

[5] A. Stogryn, "The Emissivity of Sea Foam at microwave frequencies," *J. Geophys. Res.*, vol. 77, pp. 1658–1666, 1972.

[6] W. Asher, Q. Wang, E. C. Monahan, and P. M. Smith, "Estimation of Air-Sea Gas Transfer Velocities from Apparent Microwave Brightness Temperature," *Mar. Technol. Soc. J.*, vol. 32, no. 2, pp. 32–40, 1998.

[7] R. de Vries, *Absorptive Bubble Separation Techniques*, R. Lemlich, Ed. New York: Academic, 1972, p. 331.

[8] L. Tsang, C.-T. Chen, A. T. C. Chang, J. Guo, and K.-H. Ding, "Dense Media Relative Transfer Based on Quasicrystalline Approximation with Applications to Passive Microwave Remote Sensing of Snow," *Radio Sci.*, vol. 35, no. 3, pp. 731–749, 2000.

[9] A. Ishimaru and Y. Kuga, "Attenuation constant of coherent field in a dense distribution of particles," *J. Opt. Soc. Amer.*, vol. 72, no. 10, pp. 1317–20, 1982.

[10] L. Tsang, C. E. Mandt, and K.-H. Ding, "Monte Carlo simulations of the extinction rate of dense media with randomly distributed dielectric spheres based on solution of Maxwell's equations," *Opt. Lett.*, vol. 17, no. 5, pp. 314–316, 1992.

[11] L. Tsang, J. A. Kong, and R. Shin, *Theory of Microwave Remote Sensing*. New York: Wiley, 1985.

[12] K.-H. Ding, C. Mandt, L. Tsang, and J. A. Kong, "Monte Carlo simulations of pair distribution functions of dense discrete random media with multiple sizes of particles," *J. Electromagn. Waves Applicat.*, vol. 6, no. 8, pp. 1015–1030, 1992.

[13] L. Tsang and J. A. Kong, "Scattering of electromagnetic waves from a dense medium consisting of correlated Mie scatterers with size distributions and applications to dry snow," *J. Electromagn. Waves Applicat.*, vol. 6, no. 3, pp. 265–286, 1992.

[14] K. H. Ding and L. Tsang, "Effective Propagation Constants and Attenuation Rates in Media of Densely Distributed Dielectric Particles with Size Distributions," *J. Electromagn. Waves Applicat.*, vol. 5, no. 2, pp. 117–142, 1991.

[15] R. J. Baxter, "Ornstein-Zernike Relation and Percus–Yevick Approximation for Fluid Mixtures," *J. Chem. Phys.*, vol. 52, pp. 4559–4562, 1970.

[16] L. Zurk, "Electromagnetic wave propagation and scattering in dense, discrete random media with application to remote sensing of snow," Ph.D. dissertation, Univ. Washington, Seattle, 1995.

[17] L. A. Klein and C. T. Swift, "An Improved Model for the Dielectric Constant of Sea Water at Microwave Frequencies," *IEEE Trans. Antennas Propagat.*, vol. AP-25, no. 1, pp. 104–111, 1977.

Jianjun Guo was born in Tianmen, Hubei Province, China. He received the B.S. degree in electrical engineering from Wuhan University, China, in 1995 and the M.S. degree in electrical engineering from the University of Science and Technology of China in 1998. He is currently pursuing the Ph.D. degree with the Department of Electrical Engineering, University of Washington, Seattle.

Leung Tsang (S'73–M'75–SM'85–F'90) was born in Hong Kong. He received the S.B., S.M., E.E., and Ph.D. degrees from the Massachusetts Institute of Technology, Cambridge.

He is currently a Professor of electrical engineering with the University of Washington, Seattle. He is co-author of the book *Theory of Microwave Remote Sensing* (New York: Wiley, 1985). His current research interests include wave propagation in random media and rough surfaces, remote sensing, opto-electronics, and computational electromagnetics.

Dr. Tsang has been Editor-in-Chief of IEEE TRANSACTIONS ON GEOSCIENCE AND REMOTE SENSING since 1996. He was the Technical Program Chairman of the 1994 IEEE Antennas and Propagation International Symposium and URSI Radio Science Meeting, the Technical Program Chairman of the 1995 Progress in Electromagnetics Research Symposium, and the General Chairman of the 1998 IEEE International Geoscience and Remote Sensing Symposium. He is a Fellow of the Optical Society of America and the recipient of the Outstanding Service Award of the IEEE Geoscience and Remote Sensing Society for 2000. He is also the Recipient of the IEEE Third Millenium Medal.

William Asher received the B.A. degree in chemistry from Reed College, Portland, OR, in 1980 and the Ph.D. degree in environmental science and engineering from Oregon Graduate Institute for Science and Technology, Beaverton, in 1987.

He was a Senior Research Scientist at Pacific Northwest National Laboratory, Sequim, WA, for five years and was then at the Joint Institute for the Study of the Atmosphere and the Ocean, University of Washington, Seattle. He is currently a Senior Oceanographer at the Applied Physics Laboratory, University of Washington.

Kung-Hau Ding, photograph and biography not available at the time of publication.

Chi-Te Chen, photograph and biography not available at the time of publication.